Polytechnic University of Catalonia

Master's Thesis

Numerical analysis of the melt-pool in Additive Manufacturing processes

Author:
Pau Gabarrell Coscojuela

Supervisor:
Prof. Michele Chiumenti
Dr. Andrey Molotnikov

Master of Science in Computational Mechanics at

School of Civil Engineering and

International Centre of Numerical Methods in Engineering

Barcelona, June 21, 2021

Abstract

In Additive manufacturing (AM) processes the melt-pool shape is related with the defect formation that affects the final mechanical behaviour. In this regard, it is essential to understand the influence of different process parameters, such as the scanning speed or the laser power, on the molten pool. For this reason, a numerical tool to accurately predict the melt pool size has been developed. The model has been implemented within an in-house HPC finite element solver that can solve coupled thermo-mechanical AM simulations. The Goldak's double ellipsoidal heat source model has been used to reproduce the power density distribution within the melt pool. Furthermore, to solve the phase-change at the melt-pool interface, the latent heat released during the transformation has been considered. To solve the resulting nonlinear problem, the Newton-Raphson method has been implemented. The model has been successfully verified and validated against the available experimental evidence. Beforehand, the double ellipsoidal parameters need to be calibrated to match the experimental results. In this regard, the energy absorptivity is found to be the most sensitive parameter for the predicted melt pool sizes.

Keywords: Additive manufacturing (AM), Melt-pool analysis, Double ellipsoidal heat source, Finite element method, Newton-Raphson method.

Acknowledgements

First, I would like to express my sincere gratitude to my project supervisors Prof. Michele Chiumenti and Dr. Andrey Molotnikov. For his advice and insight about AM processes that help me improve this thesis. Also, I would like to thank my colleague Carlos Moreira for his countless suggestions and support.

Besides my advisers, I would like to acknowledge the *International Center for Numerical Methods in Engineering* (CIMNE) for giving me the opportunity to be a member of their staff. Also, my sincere gratitude to *RMIT Centre for Additive Manufacturing* in Melbourne for providing me the experimental data used during this work.

Last, but not least, I would like to express my deep appreciation to my family and friends. For his encouragement and support during this project.

Contents

List of Figures

List of Tables

1 Introduction

In this section the subject studied is briefly introduced. First, the main motivations for this work are described. Then, the scope of the project and the outline of the report are explained.

1.1 Motivation

Additive manufacturing (AM) is a growing industrial technology used to produce high-performance parts through a layer-by-layer material deposition. For metallic materials, mainly two types of AM processes are used; powder bed fusion (PBF) and direct energy deposition (DED). In PBF, the powder particles are melted using a high energy source and sintered in a powder bed which forms the building layers. On the other hand, during DED processes, the metal powder is blown into the laser beam, which fuses the particles with a substrate creating a melting pool (Fig. 1). Both powders and filler wires are used as feedstock materials in DED. Besides, different types of high energy sources such as laser or electron beams are used to melt the material.

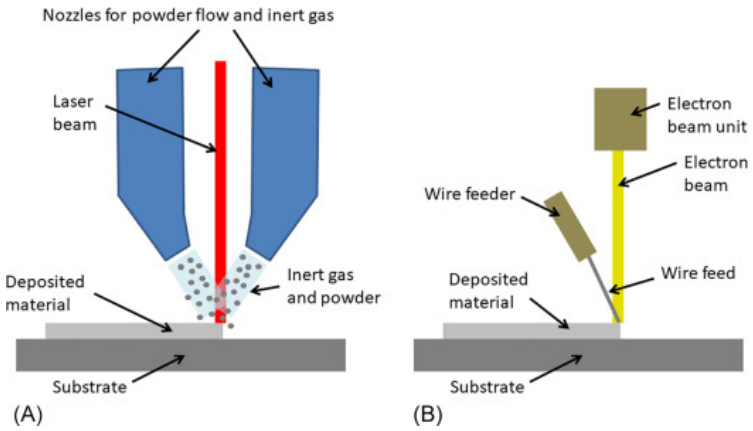

Figure 1: DED processes using (A) laser beam with powder feedstock and (B) electron beam with wire feeder [1].

The key advantages of AM in front of other metal forming technologies such as casting, consists in the process flexibility which allows for customized design in short production times. Thus, complex shapes with very thin walls or inner cavities can be produced using AM technologies. Its many different applications go from the aerospace to the biomedical industries, where it is used to produce turbine blades, aircraft stiffeners and medical implants.

The final properties of AM parts depend on the resultant transient temperature field, the solidification conditions and the microstructure evolution of the material.

A large number of AM process variables, such as the type of heat source, the scanning pattern, the hatch spacing or the powder properties influence the complex AM thermo-mechanical phenomena [4]. Thus, AM parts are normally produced and certified by trial and error for each individual component, material and AM process variant. To improve the AM design, efficient and reliable numerical tools that can model the AM process are required. Therefore, the development of mechanistic models that can accurately predict the defect formation or the solidification structure given any process parameters are crucial in AM technologies. In comparison with experimental techniques, the numerical simulations can provide detailed information within the melting pool, needed for the prediction of residual stresses, distortions and grain structure and texture.

The shape and thermal history of the molten pool is directly related with the defect formation [3]. Thus, the high temperature gradients around the heat source produce residual stresses and plastic deformations which affect the mechanical behaviour of the final component. While particle based models exists, normally thermo-mechanical continuum models are used to solve the melt-pool [5]. In this way, a great number of different phenomena can be modelled such as the liquid metal convection, the Marangoni effect or the vaporization. Typically, the finite element (FE) method is used to solve AM simulations [6].

The heat source characterization is critical to accurately reproduce the melt-pool shape in AM processes. Both the geometry and the power density distribution are crucial to predict the solidification structure and the thermal cycles within the molten pool. The first heat source models were developed for welding analysis. First, a surface heat flux with a disc shape was proposed by Pavelic [3]. However, for high energy sources such as the laser or the electron beam, the surface disc model ignores the laser digging action that transports heat well below the surface. To solve that, a volume heat source was proposed instead. The idea was to impose a Gaussian power density distribution within an ellipsoidal volume. In early 1980s, Goldak realized that the ellipsoidal power density distribution was not modelling accurately the melt pool shape. The calculation experience with the ellipsoidal heat source model revealed that the temperature gradient in front of the heat source was not as steep as expected and the gentler gradient at the trailing edge of the molten pool was steeper than the experimental evidence [3]. To overcome this limitation, two ellipsoidal sources are combined in the double ellipsoidal heat source model.

1.2 Objectives

This project aims at developing a numerical model to accurately predict the melt-pool shape in AM processes. The model is implemented within the HPC finite element solver FEMUSS, developed at the *International Center for Numerical Methods in Engineering* (CIMNE) in Barcelona. The software is capable of solving AM coupled thermo-mechanical simulations. Nevertheless, only the thermal analysis will be addressed during this work. First, the Goldak's double ellipsoidal heat source model will be developed to reproduce the laser power distribution within the melt pool.

Furthermore, to solve the phase-change at the melt-pool interface, the latent heat released during the transformation will be considered in the thermal analysis. Given the high energy source and the phase change, the resulting heat transfer problem is highly nonlinear. To solve that, the Newton-Raphson method will be implemented. Thus, the temperature dependent properties and the latent heat terms will be linearised. Once the computational framework is properly tested, the numerical model will be validated against experimental data from the *RMIT Centre for Additive Manufacturing* in Melbourne. Therefore, the melt-pool sizes will be computed and compared with the available experimental evidence.

1.3 Outline

The present report is organized as follows. First, in Sec. 2, the methodology used in this study is introduced. Starting from the balance of energy equation, the numerical formulation to solve the melt-pool in AM processes is presented. The finite element discretisation is explained step-by-step until obtaining the fully discrete form. The double ellipsoidal heat source model is explained in detail in Sec. 2.1.3. In addition, the nonlinear solver and the main implementation details are discussed in Sec. 2.4 and 2.5. Finally, the computational models used for validation are presented in Sec. 2.6 and 2.7, addressing the meshing strategy and the boundary conditions used. In Sec. 3, the main results are presented and discussed. A mesh convergence study and a time discretization study are performed in Sec. 3.2 and 3.3. After that, the model is validated against Goldak's results and experimental data in Sec. 3.5 and 3.6. Lastly, based on the presented results, final conclusions are drawn.

2 Methodology

The methodology followed in this study consists in two different parts. First, the computational framework used to solve the molten pool in AM is presented. Starting from the strong form of the problem, the finite-element formulation is introduced until obtaining the fully discrete form. Once the simulation environment is introduced, the second part consists in developing the computational models needed to validate the results.

2.1 Strong Form

The strong form of the problem can be obtained using the balance of energy equation as follows:

$$\dot{H} = -\nabla \cdot \mathbf{q} + \dot{Q} \tag{1}$$

where $\dot{H}$ and $\dot{Q}$ represent the enthalpy rate and the power source per unit of volume and $\mathbf{q}$ is the heat flux vector per unit of surface which can be expressed using the Fourier's law:

$$\mathbf{q} = -k(T)\nabla T \tag{2}$$

where $k(T)$ is the temperature dependent thermal conductivity and the negative sign indicates that the heat flux goes from high to low temperatures. The enthalpy $H(T, f_L)$ is defined as a state variable which depends on the temperature, T, and the liquid fraction, f_L. Therefore, the enthalpy rate can be expressed as [6]:

$$\dot{H}(T, f_L) = \frac{\partial H}{\partial T}\,\dot{T} + \frac{\partial H}{\partial f_L}\dot{f}_L = C(T)\dot{T} + L\dot{f}_L \tag{3}$$

where $C(T)$ is the temperature dependent heat capacity and L is the latent heat released during the phase-change process. The heat capacity is usually obtained as $C(T) = \rho c(T)$ where ρ is the material density and $c(T)$ is the specific heat capacity.

Consider a bounded domain $\Omega \subset R^d$, where d is the number of spatial dimensions, closed by the boundary Γ. The temperature distribution in time and space can be obtained solving the strong form of the problem as follows:

$$\begin{cases} \rho c\dfrac{\partial T}{\partial t} + L\dfrac{\partial f_L}{\partial t} - \nabla \cdot (k\nabla T) = \dot{Q} & \text{in } \Omega \times (0, t_{end}], \\ T = T_0 & \text{in } \Omega \times \{0\}, \\ -k\nabla T \cdot \mathbf{n} = q_{rad} + q_{conv} & \text{on } \Gamma \times (0, t_{end}], \end{cases} \tag{4}$$

where T_0 is the temperature initial condition at $t = 0$, $\mathbf{n}$ is the unit normal vector, q_{rad} and q_{conv} are the radiation and convection heat fluxes at the boundary and t_{end} denotes the final time of interest. The problem is nonlinear due to the temperature dependent properties $k(T)$ and $c(T)$ as well as the latent heat term. Notice that the liquid fraction $f_L(T)$ depends on the temperature, introducing a further non linearity into the problem.

2.1.1 Latent Heat

Since the phase-change for metals is non-isothermal, the sudden enthalpy increase during the melting process is defined between the solidification temperature T_S and the liquid temperature T_L. During the phase transformation the material volume, V, can be split into the liquid and solid phases volumes, V_L and V_S. The liquid and solid fractions represent the phase volume with respect to the total volume, $f_L = \frac{V_L}{V}$ and $f_S = \frac{V_S}{V}$, so that $f_L + f_S = 1$. Therefore, the evolution of the liquid fraction, $\dot{f}_L$, defines the phase-change, that is, how the latent heat is absorbed or released during the transformation. For our purposes, the liquid fraction is assumed linear between the solid and liquid temperatures:

$$f_L(T) = \begin{cases} 0 & \text{for} \quad T < T_S \\ \dfrac{T - T_S}{T_L - T_S} & \text{for} \quad T_S \leq T \leq T_L \\ 1 & \text{for} \quad T > T_L \end{cases} \tag{5}$$

2.1.2 Boundary Conditions

The boundary conditions represent the amount of heat lost due to convection and radiation mechanisms. The radiation and convection heat fluxes are defined as follows:

$$q_{rad} = \sigma\varepsilon(T^4 - T_{env}^4) \tag{6}$$

$$q_{conv} = h(T - T_{env}) \tag{7}$$

where σ is the Stefan-Boltzmann constant, ε is the material emissivity, $h(T)$ is the temperature dependent heat convection coefficient which will be assumed constant and T_{env} is the surrounding environment temperature. Notice that far from the scanning path the heat loses due to convection and radiation will decrease until zero.

2.1.3 Heat Source

In additive manufacturing processes, the heat source $\dot{Q}$ from Eq. 4 can be approximated as a Gaussian distribution within an ellipsoid which is moving with a constant speed [4]. The center of the ellipsoid corresponds with the laser position at each time step. Notice that in this way, the heat source $\dot{Q}(x, y, z, t)$ depends on both time and space. It can also be expressed with a coordinate system that moves in the x direction with the heat source using the following transformation:

$$\xi = x + v(\tau - t) \tag{8}$$

where ξ is the first ellipsoidal coordinate, v is the scanning speed and τ is a parameter needed to define the initial heat source position. Therefore, the Gaussian distribution of the power density in an ellipsoid can be written as:

$$\dot{Q}(\xi, y, z) = q_0\, e^{-A\xi^2} e^{-By^2} e^{-Cz^2} \tag{9}$$

where q_0 is the maximum value of the power density at the center of the ellipsoid and A, B, and C are different constants that define the power Gaussian distribution. Using the conservation of energy, all the net input power needs to be distributed within the ellipsoid as follows:

$$\eta P = 4 \int_0^a \int_0^b \int_0^c q_0 \, e^{-A\xi^2} e^{-By^2} e^{-Cz^2} \mathrm{d}\xi \, \mathrm{d}y \, \mathrm{d}z \tag{10}$$

where P is the input power in watts, η is the energy absorptivity parameter and a, b and c are the ellipsoid axes. Solving the integral from Eq. 10:

$$\eta P = \frac{q_0 \pi \sqrt{\pi}}{2\sqrt{ABC}} \operatorname{erf}(\sqrt{A}a) \operatorname{erf}(\sqrt{B}b) \operatorname{erf}(\sqrt{C}c) \tag{11}$$

where $\operatorname{erf}(x)$ is the Gauss error function. The constants A, B and C are defined such that the power density falls to 5% at the surface of the ellipsoid. Therefore,

$$\dot{Q}(a, 0, 0) = q_0 e^{-Aa^2} = 0.05 q_0 \tag{12}$$

Giving,

$$A = \frac{\ln 20}{a^2} \simeq \frac{3}{a^2} \tag{13}$$

Similarly,

$$B = \frac{3}{b^2} \qquad C = \frac{3}{c^2} \tag{14}$$

Substituting Eq. 13 and 14 into Eq. 11, an expression for q_0 is obtained:

$$q_0 = \frac{\eta P 6\sqrt{3}}{abc \, \pi \sqrt{\pi}} \, \phi \tag{15}$$

where ϕ is a volume correction factor that appears because the power density is evaluated on the finite domain enclosed by the ellipsoid. If the power density would have been evaluated on an infinite domain, then $\lim_{x\to\infty} \operatorname{erf}(x) = 1$ giving $\phi = 1$. Therefore, when the power density is only evaluated inside the region defined by the ellipsoid, the maximum power q_0 needs to be corrected to ensure the conservation of energy. Evaluating the Gauss error functions from Eq. 11,

$$\phi = \operatorname{erf}(\sqrt{3})^{-3} \simeq 1.0442 \tag{16}$$

Finally, the expression from Eq. 15 is introduced into the initial Gaussian distribution in Eq. 9. The ellipsoidal heat source distribution is obtained undoing the change of variables in Eq. 8.

$$\dot{Q}(x, y, z, t) = \frac{\eta P 6\sqrt{3}}{abc \, \pi \sqrt{\pi}} \phi \, e^{-3[x+v(\tau-t)]^2/a^2} e^{-3y^2/b^2} e^{-3z^2/c^2} \tag{17}$$

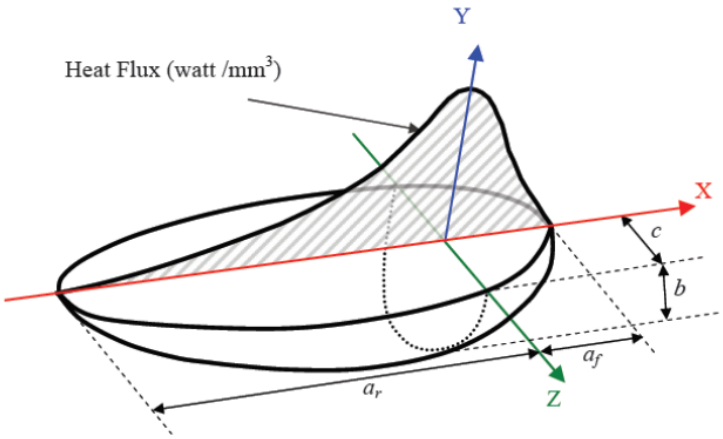

Figure 2: Goldak's double ellipsoidal heat source model [2].

In early 1980s, Goldak introduced a double ellipsoidal power density distribution combining two ellipsoids (Fig. 2). The idea is that the front and rear half of the heat source, $\dot{Q}_f$ and $\dot{Q}_f$, are modelled using different Gaussian distributions as follows [3]:

$$\dot{Q}_f(\xi, y, z) = \frac{\eta f_f P 6\sqrt{3}}{a_f bc\,\pi\sqrt{\pi}} \phi\, e^{-3\xi^2/a_f^2} e^{-3y^2/b^2} e^{-3z^2/c^2} \tag{18}$$

$$\dot{Q}_r(\xi, y, z) = \frac{\eta f_r P 6\sqrt{3}}{a_r bc\,\pi\sqrt{\pi}} \phi\, e^{-3\xi^2/a_r^2} e^{-3y^2/b^2} e^{-3z^2/c^2} \tag{19}$$

where f_f and f_r are the power fractions corresponding to the front and rear ellipsoids and a_f and a_r are the front and rear ellipsoid axis. Notice that the two Gaussian distributions need to be continuous at the mid plane $\xi = 0$.

$$\dot{Q}_f(0, y, z) = \dot{Q}_r(0, y, z) \tag{20}$$

Giving the following relation between the power fractions, f_f and f_r, and the ellipsoid axis, a_f and a_r [2]:

$$\frac{f_f}{a_f} = \frac{f_r}{a_r} \tag{21}$$

Besides, it can be proven that the power fractions need to sum 2 to follow the conservation of energy in Eq. 10 [3].

$$f_f + f_r = 2 \tag{22}$$

Combining Eq. 21 and 22, an expression for the power fractions f_f and f_r is obtained:

$$f_f = \frac{2\,a_f}{a_f + a_r} \qquad f_r = \frac{2\,a_r}{a_f + a_r} \tag{23}$$

2.2 Weak form

To solve the strong form, the following discrete functional space is introduced:

$$\mathcal{W}^h(\Omega) := \left\{ W \in \mathcal{L}_2(\Omega) : W|_\Omega \in \mathcal{P}^k(\Omega) \right\} \tag{24}$$

where $\mathcal{P}^k(\Omega)$ denotes the space of polynomial functions of complete degree at most k in Ω. The weak form is obtained integrating Eq. 4 over the domain Ω and multiplying by the test function w.

$$\int_\Omega w\left[\rho c\frac{\partial T}{\partial t}+L\frac{\partial f_L}{\partial t}\right]d\Omega-\int_\Omega w\nabla\cdot(k\nabla T)d\Omega=\int_\Omega w\dot{Q}d\Omega \tag{25}$$

Applying the chain rule to the second integral in the left hand side,

$$\int_\Omega w\left[\rho c\frac{\partial T}{\partial t}+L\frac{\partial f_L}{\partial t}\right]d\Omega+\int_\Omega \nabla w\cdot(k\nabla T)d\Omega=\int_\Omega w\dot{Q}d\Omega+\int_\Omega \nabla\cdot(wk\nabla T)d\Omega \tag{26}$$

Applying the divergence theorem to the second integral in the right hand side, the normal heat flux boundary condition is recovered on the boundary Γ [7].

$$\int_\Omega w\left[\rho c\frac{\partial T}{\partial t}+L\frac{\partial f_L}{\partial t}\right]d\Omega+\int_\Omega \nabla w\cdot(k\nabla T)d\Omega=\int_\Omega w\dot{Q}d\Omega+\int_\Gamma w(k\nabla T\cdot\mathbf{n})\,d\Gamma \tag{27}$$

Finally, the weak form of the problem reads: find $T\in\mathcal{L}_2\left((0,t_{end}];\mathcal{W}^h(\Omega)\right)$ such that

$$\int_\Omega w\left[\rho c\frac{\partial T}{\partial t}+L\frac{\partial f_L}{\partial t}\right]d\Omega+\int_\Omega \nabla w\cdot(k\nabla T)d\Omega=\int_\Omega w\dot{Q}d\Omega-\int_\Gamma w(q_{rad}+q_{conv})d\Gamma \tag{28}$$

for all $w\in\mathcal{L}_2\left((0,t_{end}];\mathcal{W}^h(\Omega)\right)$.

2.3 Discrete form

The spatial discretisation is performed using first-order isoparametric hexahedral elements. The nonlinear semi-discrete form can be written as

$$\mathbf{M}(\mathbf{T})\frac{d\mathbf{T}}{dt}+\frac{d\mathbf{L}(\mathbf{T})}{dt}+\mathbf{K}(\mathbf{T})\mathbf{T}=\dot{\mathbf{Q}}-\mathbf{B}(\mathbf{T}) \tag{29}$$

where $\mathbf{T}$ is the vector containing the nodal values of the temperature, $\mathbf{M}$ is the temperature dependent mass matrix, $\mathbf{L}$ is the latent heat vector, $\mathbf{K}$ is the temperature dependent Laplacian matrix, $\dot{\mathbf{Q}}$ is the heat source vector and $\mathbf{B}$ represents the nonlinear boundary conditions contribution.

$$\mathbf{M}_{IJ}=\int_\Omega \rho c(T)N_IN_Jd\Omega \tag{30a}$$

$$\mathbf{L}_I=\int_\Omega N_ILf_L(T)d\Omega \tag{30b}$$

$$\mathbf{K}_{IJ}=\int_\Omega \nabla N_Ik(T)\nabla N_Jd\Omega \tag{30c}$$

$$\dot{\mathbf{Q}}_I=\int_\Omega N_I\dot{Q}d\Omega \tag{30d}$$

$$\mathbf{B}_I=\int_\Gamma N_I\left[q_{rad}(T)+q_{conv}(T)\right]d\Gamma \tag{30e}$$

An implicit time discretisation is proposed to approximate the temporal derivatives in Eq. (29). Introducing the first-order backward Euler method (BDF1), the fully discrete residual at time $t = t^{n+1}$ is obtained:

$$\begin{aligned}\mathbf{R}^{n+1} := \mathbf{M}(\mathbf{T}^{n+1})(\mathbf{T}^{n+1} - \mathbf{T}^{n}) + \mathbf{L}(\mathbf{T}^{n+1}) - \mathbf{L}(\mathbf{T}^{n}) + \Delta t \left(\mathbf{K}(\mathbf{T}^{n+1})\mathbf{T}^{n+1}\right) \\ \Delta t \left(-\dot{\mathbf{Q}}^{n+1} + \mathbf{B}(\mathbf{T}^{n+1})\right) = \mathbf{0}\end{aligned} \tag{31}$$

2.4 Nonlinear solver

The resulting nonlinear residual from Eq. 31 needs to be linearized in order to obtain a linear system of equations. Two different nonlinear solvers have been studied: the Newton-Raphson method and the Picard's method.

2.4.1 Picard's Method

The Picard's method approximates all the nonlinear terms from the residual in Eq. 31 using the solution from the previous iteration. So, the solution $\mathbf{T}_{i+1}^{n+1}$ at iteration $i+1$ is obtained solving the following linear system which depends on the known solution $\mathbf{T}_{i}^{n+1}$ and $\mathbf{T}^{n}$:

$$\mathbf{A}(\mathbf{T}_{i}^{n+1})\,\mathbf{T}_{i+1}^{n+1} = \mathbf{b}(\mathbf{T}_{i}^{n+1}, \mathbf{T}^{n}) \tag{32}$$

with

$$\mathbf{A}(\mathbf{T}_{i}^{n+1}) = \mathbf{M}(\mathbf{T}_{i}^{n+1}) + \Delta t \mathbf{K}(\mathbf{T}_{i}^{n+1}) \tag{33}$$

$$\mathbf{b}(\mathbf{T}_{i}^{n+1}, \mathbf{T}^{n}) = \Delta t \left(\dot{\mathbf{Q}}^{n+1} - \mathbf{B}(\mathbf{T}_{i}^{n+1})\right) + \mathbf{M}(\mathbf{T}_{i}^{n+1})\mathbf{T}^{n} + \mathbf{L}(\mathbf{T}^{n}) - \mathbf{L}(\mathbf{T}_{i}^{n+1}) \tag{34}$$

2.4.2 Newton-Raphson Method

The Newton-Raphson (NR) method computes the exact Jacobian matrix to linearize the residual at t^{n+1} as follows:

$$\left[\frac{d\mathbf{R}(\mathbf{T})}{d\mathbf{T}}\right]_{i}^{n+1} \Delta\mathbf{T}_{i+1}^{n+1} = -\mathbf{R}_{i}^{n+1} \tag{35}$$

where the incremental solution $\Delta\mathbf{T}_{i+1}^{n+1}$ at iteration $i+1$ is obtained solving a linear system using the known solution $\mathbf{T}_{i}^{n+1}$ from the previous iteration. Then, the solution is updated as follows

$$\mathbf{T}_{i+1}^{n+1} = \Delta\mathbf{T}_{i+1}^{n+1} + \mathbf{T}_{i}^{n+1} \tag{36}$$

Notice that the Newton-Raphson method can also be formulated using a non-incremental form analogous to the Picard's method in Eq. 32.

$$\left[\frac{d\mathbf{R}(\mathbf{T})}{d\mathbf{T}}\right]_{i}^{n+1} \mathbf{T}_{i+1}^{n+1} = -\mathbf{R}_{i}^{n+1} + \left[\frac{d\mathbf{R}(\mathbf{T})}{d\mathbf{T}}\right]_{i}^{n+1} \mathbf{T}_{i}^{n+1} \tag{37}$$

The Jacobian matrix from Eq. 35 can be obtained as

$$\frac{d\mathbf{R}(\mathbf{T})}{d\mathbf{T}} = \frac{d\mathbf{M}(\mathbf{T})}{d\mathbf{T}} \cdot \mathbf{T} + \mathbf{M} + \frac{d\mathbf{L}(\mathbf{T})}{d\mathbf{T}} + \Delta t \left(\frac{d\mathbf{K}(\mathbf{T})}{d\mathbf{T}} \cdot \mathbf{T} + \mathbf{K} \right) \tag{38}$$

with [8]

$$\left(\frac{d\mathbf{M}}{d\mathbf{T}} \cdot \mathbf{T} \right)_{IJ} = \int_{\Omega} N_I \, \rho \, \frac{dc}{dT} \, T \, N_J d\Omega \tag{39a}$$

$$\left(\frac{d\mathbf{L}}{d\mathbf{T}} \right)_{IJ} = \int_{\Omega} N_I L \, \frac{df_L}{dT} \, N_J d\Omega \tag{39b}$$

$$\left(\frac{d\mathbf{K}}{d\mathbf{T}} \cdot \mathbf{T} \right)_{IJ} = \int_{\Omega} \nabla N_I \, \frac{dk}{dT} \, \nabla T \, N_J d\Omega \tag{39c}$$

Remark 1 *Notice that in Eq. 38, the boundary conditions term* $\mathbf{B}$ *has not been linearized. Instead, the nonlinear radiation heat flux,* q_{rad}*, is treated using the Picard's method and evaluated at the previous iteration. The convection heat flux,* q_{conv}*, is linear and therefore does not need any linerization strategy.*

Remark 2 *The Newton-Raphson non-incremental form in Eq. 37 has been selected for the implementation. The main idea is to obtain a linear system analogous with the Picard's method to simplify the implementation. Thereby, the* $\mathbf{M}$ *and* $\mathbf{K}$ *terms in Eq. 38 are canceled with the residual in the right hand side of Eq. 37.*

2.5 Implementation Details

To illustrate the decisions made during the development, the main implementations details regarding the double ellipsoidal heat source and the Newton-Raphson linearisation terms are going to be explained.

2.5.1 Double Ellipsoidal Heat Source

Before starting the computations, the double ellipsoidal parameters (a_f, a_r, b, c, f_f and f_r) are calculated using the estimated melt pool size input values. At each time step, the new heat source position, $\mathbf{x}^{n+1}$, is computed. Then, the power density $\dot{Q}^{n+1}$ is evaluated at the gauss points for each element inside the melt pool (Algorithm 1).

To select which elements are inside the double ellipsoidal at each time step, the `MeltPoolBox` is defined. It is a hexahedral domain with sides $a_f + a_r$, $2b$ and c that contains the double ellipsoidal (Fig. 2). Using a face intersection algorithm, the elements inside the `MeltPoolBox` are determined. Notice that the expressions to compute the power density in Eq. 18 and 19 are using a local coordinate system that moves with the heat source. Therefore, a change of variables from the global to the ellipsoidal coordinates is needed (Algorithm 1).

Remark 3 *A common alternative to define the heat source is to use a constant power density within the melt pool [9]. First, the elements inside the melt pool are*

Algorithm 1: Compute double ellipsoidal heat source

Input: $\mathbf{x}^{n+1}$, a_f, a_r, b, c, f_f, f_r
Output: $\dot{Q}^{n+1}$
MeltPoolBox $\leftarrow$ `BuildMeltPoolBox`($\mathbf{x}^{n+1}$, a_f, a_r, b, c)
for $e \leq$ *nOfElem* **do**
  inside $\leftarrow$ `isElementInsideMeltPoolBox`(e, MeltPoolBox)
  if inside **then**
    for $g \leq$ *nOfGaussPoints* **do**
      $\boldsymbol{x}_{gaus} \leftarrow$ `GetGaussCoord`(e, g)
      $\boldsymbol{x}_{ellip} \leftarrow$ `GaussToEllipsoidCoord`(MeltPoolBox, $\boldsymbol{x}_{gaus}$)
      if $\boldsymbol{x}_{ellip}(1) \geq 0$ **then**
        $P^* \leftarrow f_f P$
        $a^* \leftarrow a_f$
      else
        $P^* \leftarrow f_r P$
        $a^* \leftarrow a_r$
      end
      $\dot{Q}^{n+1}(e, g) \leftarrow$ `EllipsoidPowerDensity`($P^*, a^*, b, c, \boldsymbol{x}_{ellip}$)
    end
  end
end

determined, computing the total volume of the melt pool, V_{MP}. The constant power density is obtained as the net input power divided by the melt pool volume as follows $\dot{Q} = \frac{\eta P}{V_{MP}}$. After that, another loop over the elements inside the melt pool is needed to assign the heat source at each element. Regarding the implementation, the double ellipsoidal model presents a clear advantage in front of the constant heat source, given that only one loop over all the elements is needed.

2.5.2 Material Properties Derivatives

The temperature dependent material properties $c(T)$ and $k(T)$ are defined using a set of discrete data. These data is linearly interpolated to compute the material properties at any given temperature, T. First, a bisection algorithm is used to find the discrete temperature values, T_i and T_{i+1}, that define the temperature interval which contains T. Thereby, any temperature dependent property, $\theta(T)$, can be calculated as follows:

$$\theta(T) = \theta_i a_i + \theta_{i+1}(1 - a_i) \quad \text{with} \quad a_i(T) = \frac{T_{i+1} - T}{T_{i+1} - T_i} \tag{40}$$

where θ_i and θ_{i+1} are the discrete property values at temperatures T_i and T_{i+1} respectively. Derivating Eq. 40 with respect to T, an expression to compute the material properties derivatives in Eq. 39 is obtained.

$$\frac{d\,\theta(T)}{dT} = \frac{\theta_{i+1} - \theta_i}{T_{i+1} - T_i} \tag{41}$$

2.5.3 Liquid Fraction Derivative

The liquid fraction, $f_L(T)$, is calculated for any given temperature, T, using Eq. 5. However, when computing its exact derivative in Eq. 39, two problems appear. The derivative is not continuous at T_S and T_L, but more important, the derivative is zero outside the phase-change temperatures. Therefore, if the temperature difference between T^{n+1} and T^n is greater than the phase-change, the latent heat linearisation term may be ignored. That is, if the time step is too large, the enthalpy jump is not considered by the Jacobian matrix. To solve that, an secant approximation of the derivative is used outside the transformation temperatures. While within the phase-change temperatures T_S and T_L, the exact constant derivative is used. Thereby, to compute the liquid fraction derivative at t^{n+1} the following algorithm has been used.

Algorithm 2: Compute liquid fraction derivative

Input: T^{n+1}, T^n T_L, T_S
Output: $\frac{df_L}{dT}^{n+1}$
if $T^{n+1} \in [T_S, T_L]$ **then**
    $\frac{df_L}{dT}^{n+1} = \frac{1}{T_L - T_S}$
else
    $f_L^n \leftarrow$ `ComputeLiquidFraction`(T^n, T_S, T_L)
    $f_L^{n+1} \leftarrow$ `ComputeLiquidFraction`(T^{n+1}, T_S, T_L)
    $\frac{df_L}{dT}^{n+1} = \frac{f_L^{n+1} - f_L^n}{T^{n+1} - T^n}$
end

2.6 Goldak's Model

To validate the simulation results, the computational model presented by Goldak in [3] has been used. It consists of a low carbon steel thick section bead-on-plate weld. The welding conditions and ellipsoid parameters used are reported in Fig. 4. In Goldak's analysis, a 2D simulation was done in the plane normal to the welding direction to reduce the computational costs, Thus, it is assumed that the heat flow in the welding direction can be neglected when the welding speed is high enough. To obtain a more general approach, a 3D model has been developed instead.

The simulation domain in Fig. 3, has been constructed to be long enough such that the steady-state solution is achieved. During the fist time steps, the material is being heated by the laser power, increasing the peak temperature within the melt pool. Once the steady-state is achieved, the melt pool size and the peak temperature remain constant as the laser moves throughout the domain. It has been found that $75\,mm$ are needed to reach the steady-state solution. Comparing it with the double ellipsoidal length, $a_r + a_f = 45\,mm$, it correspond to 1.6 times the heat source length. It has been noticed that the solution is not completely steady outside the melt pool region. In fact, the heat affected zone behind the laser keeps growing far

from the melt as the laser advances.

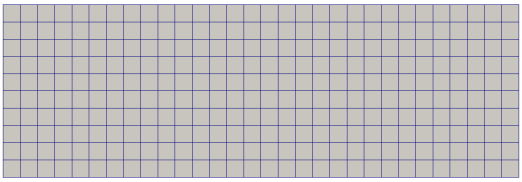

(a) Initial coarse mesh

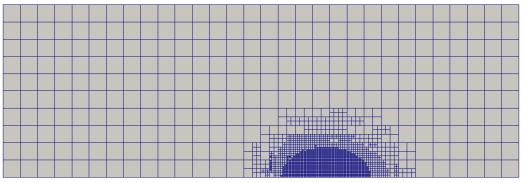

(b) Refined mesh around the melt-pool

Figure 3: Octree-based adaptive mesh refinement with 4 levels of refinement (view from the top).

A structured hexahedral mesh has been used with an octree-based adaptive mesh refinement. The idea is to reduce the computational costs by using a coarse mesh with $h = 10\,mm$ far from the melt pool. At the same time, a really small grid is used around the melt pool to properly capture the phase-change (Fig. 3). The mesh is hierarchically refined using different levels of refinement. Thus, an error estimator is used to determine if further mesh refinement is needed around the melt pool at each time step. Besides, a coarsening criteria is used to keep the number of elements constant as the double ellipsoidal heat source is moving throughout the domain. An efficient load-rebalanced adaptive mesh refinement algorithm for high performance computing has been used [10].

2.6.1 Boundary Conditions

In Goldak's model, all faces except the top surface are assumed insulated. Thus, the normal heat flux, q_n, is set to zero. In addition, a symmetry boundary condition is used at the middle plane to model only half of the melt pool. On the top surface, a combination of convection and radiation loses is considered imposing the following normal heat flux:

$$q_n = H\,(T - T_{env}) \quad \text{with} \quad H(T) = 24.1 \times 10^{-4} \varepsilon T^{1.61} \tag{42}$$

where H is a combined heat transfer coefficient and the emissivity is set to $\varepsilon = 0.9$. Besides, in Goldak's analysis, the portion just under the welding arc was assumed insulated during the time the arc was playing upon the surface. In other words, no loses were considered on the double ellipsoidal top surface. To reproduce the same

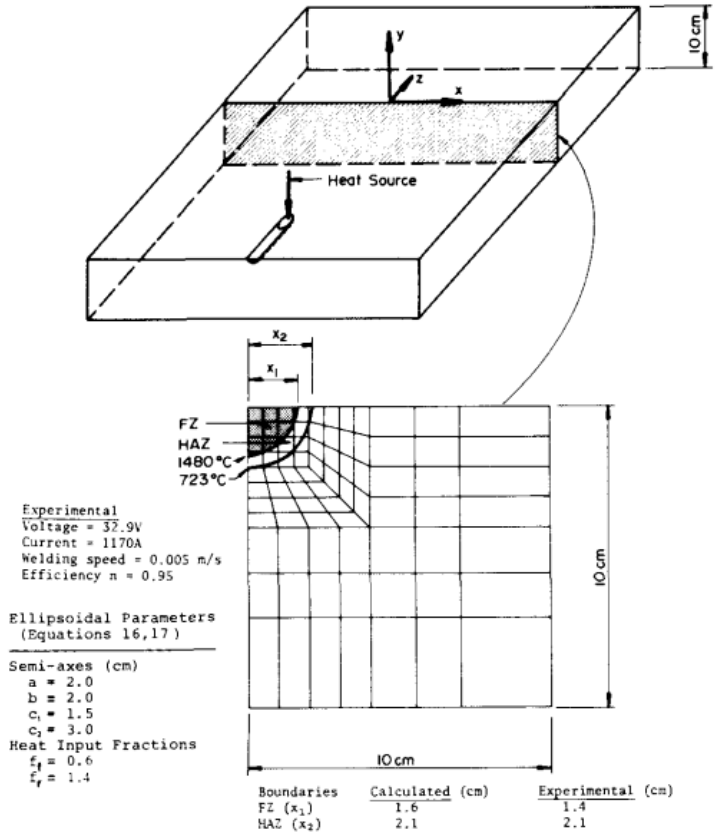

Figure 4: Goldak's computational model with the ellipsoidal parameters used and the welding experimental conditions [3].

boundary conditions, the heat convection coefficient, h, from Eq. 7 has been calibrated to match Goldak's loses. Therefore, in Fig. 5, the convection and radiation boundary conditions are compared with Goldak's normal heat flux in Eq. 42.

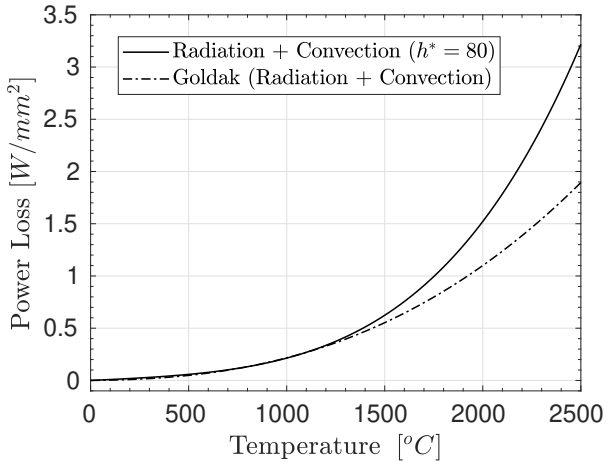

Figure 5: Comparison between Goldak's heat loses and the radiation and convection boundary conditions.

Assuming a constant heat convection coefficient, the Goldak's heat loses are accurately predicted up to approximately $T = 1400°C$. For higher temperatures, the fourth-order radiation boundary condition increases the heat loses beyond Goldak's expression. Nevertheless, Goldak's model is not considering any loses on the double ellipsoid top surface, so it is reasonable to assume that beyond the solid temperature, T_S, no loses occur. Thus, to match Goldak's boundary conditions, the heat convection coefficient and the radiation emissivity are set to zero inside the melt pool. The following expressions are used to validate Goldak's model.

$$h(T) = \begin{cases} 80 & \text{for} \quad T \leq T_S \\ 0 & \text{for} \quad T > T_S \end{cases} \qquad \varepsilon(T) = \begin{cases} 0.9 & \text{for} \quad T \leq T_S \\ 0 & \text{for} \quad T > T_S \end{cases} \tag{43}$$

2.6.2 Material Properties

The relevant low carbon steel material properties are taken from [3] and presented in Fig. 6 and Tab. 1.

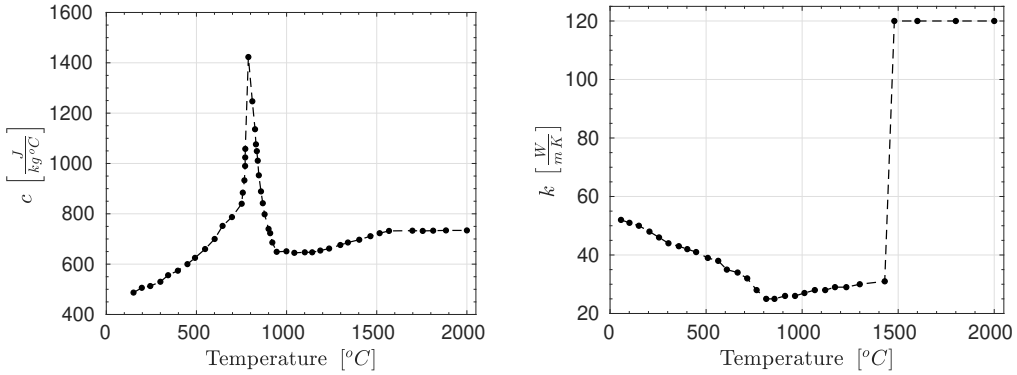

(a) Specific Heat Capacity (b) Thermal Conductivity

Figure 6: Low carbon steel material properties.

Density $[kg/m^3]$	Latent Heat $[J/kg]$	Solid/Liquid Temperature $[°C]$
7850	2.67×10^5	1430 - 1480

Table 1: Low carbon steel material properties.

Notice how the specific heat capacity in Fig. 6 presents a remarkable peak around the transformation temperature which introduces a highly non-linearity. At the solid temperature, the specific heat remains constant because the heat of fusion is already being considered using the latent heat. The thermal conductivity at the liquid phase is set to $k = 120\,W/m°C$, to reproduce the convection heat transfer effects within the fusion zone. Finally, the density is assumed constant to fulfill the conservation of mass at all times.

2.7 Experimental Model

The presented double ellipsoidal heat source model has been validated against experimental data provided by the RMIT Centre for Additive Manufacturing in Melbourne. The model's ability to accurately predict the melt pool shape has been tested using different operating conditions. Using direct energy deposition (DED), different tracks have been produced and analysed (Fig. 7). The melt pool depth ad width have been measured using different laser powers and transverse speeds. The experimental substrate samples consists of Ti-6Al-4V titanium alloy plates with dimensions 200 mm long, 100 mm wide and 4.1 mm thick. The plate surfaces have been wiped with acetone before the process. Besides, a coaxial nozzle has been used with Ti-6Al-4V powder. The main experimental parameters are detailed in Tab. 2.

Powder Feed Rate	3 rpm
Powder Flow Rate	2.27 g/min
Laser Spot Size	2.5 mm
Carrier Gas (Helium)	10 L/min
Shielding Gas (Argon)	16 L/min

Table 2: Experimental global build parameters.

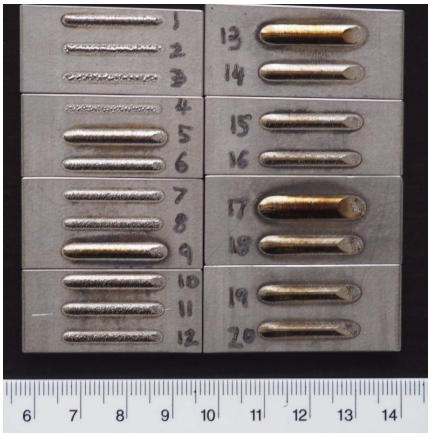

Figure 7: Experimental tracks produced with DED using Ti-6Al-4V alloy.

The computational model to validate the experimental evidence has been build using the previous experience with Goldak's model. Thus, the same meshing strategy has been used, as well as the boundary conditions detailed in Sec. 2.6. However, the double ellipsoidal heat source parameters have been changed to accurately reproduce the experimental results. The a_f and c ellipsoidal axes have been determined using the laser spot size in Tab. 2. The optimal front and rear power fractions, f_f and f_r, found by Goldak in [3] have been used. Using the continuity condition from Eq. 21, the rear ellipsoid axis, a_r, has been computed. Finally, the energy absorptivity, η, and the ellipsoid depth, b, have been calibrated to match the experimental evidence. The parameters used are detailed in Tab. 3.

$a_f\,[mm]$	$a_r\,[mm]$	$b\,[mm]$	$c\,[mm]$	f_f	f_r	η
2.5	5.83	0.3	2.5	0.6	1.4	0.6/0.78

Table 3: Double ellipsoidal heat source parameters.

To calibrate the double ellipsoidal model, a single experimental track has been simulated using different values for η and b. The melt pool results have been compared with the experimental data to chose the most accurate parameter combination. The

double ellipsoidal axis and the power fractions in Tab. 3 represent how the laser power is spread into the domain and are expected to remain independent from the operating conditions. The heat source shape will highly depend on the additive technology used, as well as different experimental parameters such as the laser spot size or the type of nozzle used. However, the absorptivity parameter which represents the amount of energy absorbed by the powder particles is found to dependent on the laser input power. Among many other parameters, the absorptivity depends on the local temperature of the material within the melt pool which is increased by the input power. Thus, a lower absorptivity is needed to match the experimental results with higher laser powers.

2.7.1 Material Properties

The relevant Ti-6Al-4V material properties are taken from [11] and presented in Fig. 8 and Tab. 4.

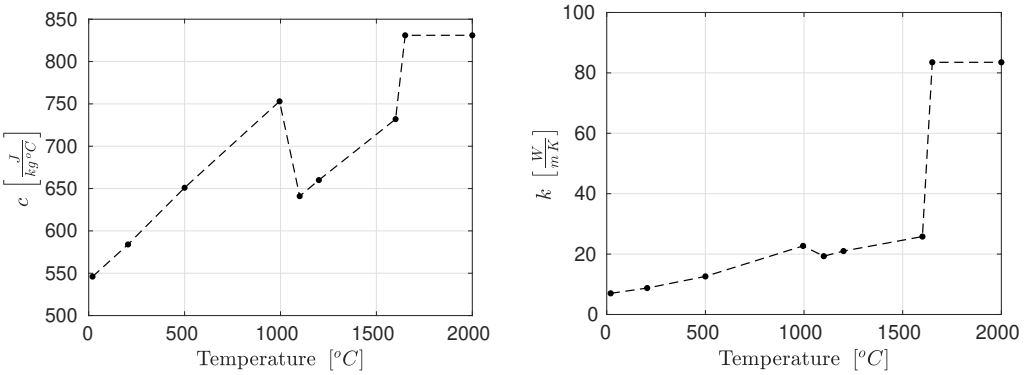

(a) Specific Heat Capacity

(b) Thermal Conductivity

Figure 8: Ti-6Al-4V material properties.

Density $[kg/m^3]$	Latent Heat $[J/kg]$	Solid/Liquid Temperature $[^\circ C]$
4420	2.9×10^5	1697 - 1703

Table 4: Ti-6Al-4V material properties.

The Ti-6Al-4V temperature dependent material properties present a similar behaviour than the low carbon steel used in Goldak's model. However, the specific heat capacity transformation peak is much less pronounced in Fig. 8, introducing a smaller non-linearity. On the other hand, the thermal conductivity phase change discontinuity is sharper in Fig. 8, given that the solid to liquid temperature difference is only $6\,^\circ C$. Therefore, really small elements are needed at the melt pool interface to properly capture the phase-change discontinuity and the latent heat effect.

3 Results and Discussion

In this section, the results obtained are presented and discussed. First, the double ellipsoidal heat source model is tested with an analytical expression. After that, the numerical model is verified studying the mesh and time convergence. The Newton-Raphson convergence is also investigated. Finally, the proposed model is validated with Goldak's original results and the available experimental evidence.

3.1 Heat Source Validation

The Goldak's double ellipsoidal heat source model defined in Sec. 2.1.3 has been validated with an analytical expression to verify that the conservation of energy holds. The idea is to define an insulated domain with no heat loses and check that the final temperature is consistent with the amount of power, P, introduced by the moving heat source. Using constant material properties, the following analytical relation can be obtained.

$$T_{end} = \frac{\eta P \Delta t}{\rho c V} + T_0 \tag{44}$$

where T_{end} is the steady state constant temperature, Δt represents the heat source scanning time, V is the domain volume and T_0 is the initial temperature. The Goldak's heat source is activated during $\Delta t = 6\,s$. Then the simulation is continued until a constant temperature is reached in all the domain. A high thermal conductivity is used to reduce the time to reach the steady state. The results are presented in Tab. 5 using different minimum element sizes, h_{min}, to discretise the melt pool. Besides, the effect of the volume correction factor, ϕ, from Eq. 16 has also been studied.

h_{min} $[mm]$	T_{end} without ϕ $[^\circ C]$		T_{end} with ϕ $[^\circ C]$	
4	47.48	-0.98%	48.68	+1.52
2	47.29	-1.38%	48.48	+1.11%
1	47.08	-1.81%	48.28	+0.68%
0.5	46.94	-2.11%	48.1	+0.31%

Table 5: Goldak's double ellipsoidal heat source validation.

The percentage errors in Tab. 5 are computed comparing the simulation results with the analytical expression in Eq. 44. It can be seen how the results with the volume correction factor are improved when the mesh is refined. On the other hand, the simulations without the volume correction factor are giving worst results when reducing the element size. As discussed in Sec. 2.1.3, the volume correction factor is needed to correct the amount of energy distributed within the double ellipsoidal. Therefore, the results without ϕ are underestimating the final temperature T_{end}. The definition of the volume correction factor in Eq. 16 assumes that the energy

is distributed within the finite domain enclosed by the double ellipsoidal. This assumption holds for fine meshes that can accurately reproduce the double ellipsoidal domain, but not for coarse meshes. As it can be seen in Tab. 5, for big element sizes T_{end} is overestimated due to the fact that the double ellipsoidal is not well resolved. The results in Tab. 5, show the importance of the mesh resolution within the melt pool to accurately reproduce the double ellipsoidal domain and fulfill the conservation of energy.

3.2 Mesh Convergence

To verify the computational model presented in Sec. 2.6, a mesh convergence study has been performed. The idea is to study the effect of different refinement levels on the melt-pool size to determine the optimal melt pool discretization. To that end, four different meshes with an adaptive mesh refinement have been used (Tab. 6). Thus, the melt-pool dimensions and the peak temperature have been computed using different meshes in Tab. 7. The melt-pool (MP) length, width and depth are calculated using the liquid temperature, T_L. The peak temperature corresponds to the maximum temperature within the melt pool. The relative error with respect to the finer mesh is also shown in Tab. 7.

	Refinement Levels	$h_{min}\,[mm]$	Number of Elements
Mesh 1	3	1.25	40×10^3
Mesh 2	4	0.625	130×10^3
Mesh 3	5	0.313	230×10^3
Mesh 4	6	0.156	540×10^3

Table 6: Minimum element size h_{min} and total number of elements for different refinement levels.

	MP Length $[mm]$		MP Width $[mm]$		MP Depth $[mm]$		Peak Temperature $[^\circ C]$	
Mesh 1	58.5	0%	13.75	7.3%	15	2%	2452	0.32%
Mesh 2	58.8	0.51%	14.38	3.1%	15	2%	2448	0.16%
Mesh 3	58.8	0.51%	14.69	1%	15.31	0%	2447	0.12%
Mesh 4	58.5	-	14.84	-	15.31	-	2444	-

Table 7: Melt pool dimensions and peak temperature mesh convergence study.

In Tab. 7, the MP width is clearly the most sensitive parameter to the mesh refinement level. Thus, the MP width increases when reducing the minimum element size at the melt pool interface. The rest of parameters in Tab. 7, present a smaller error that can be accepted. Notice that the optimal mesh is determined by balancing the computational cost, which increases dramatically with the number of refinement levels, with the solution accuracy. The Mesh 2 with $h_{min} = 0.625$ has been selected to validate the simulation results. It presents a maximum error of 3.1% in front of the finer mesh used, but the computational costs are greatly reduced from half million of elements to 100 thousand. Of course, the number of elements depends also

on the domain length, which in Goldak's model is build to achieve the steady-state solution.

3.3 Time Convergence

The time discretization is studied to determine which is the maximum welding step that can be used without compromising the solution accuracy. A larger welding step is desired to reduce the number of time steps required to achieve the steady-state solution. Thus, the MP dimensions and the peak temperature are computed using different welding steps Δx in Tab. 8. The welding step represents the distance that the heat source is moving at each time step. Therefore, it is directly related to the time step, Δt, and the welding velocity, v, as follows $\Delta x = \Delta t\, v$. The relative error with respect to the smaller time step is also shown in Tab. 8.

Δx $[mm]$	MP Length $[mm]$		MP Width $[mm]$		MP Depth $[mm]$		Peak Temperature $[°C]$	
10*	72.3	5.7%	14.38	4.1%	14.38	4.1%	2413	4.6%
5*	67.2	1.8%	14.38	4.1%	15	0%	2467	2.5%
2	69.3	1.3%	15	0%	15	0%	2511	0.8%
1	68.1	0.4%	15	0%	15	0%	2525	0.2%
0.5	68.4	-	15	-	15	-	2534	-

Table 8: Melt pool dimensions and peak temperature time convergence study.

The larger welding steps, $\Delta x = 10\,mm$ and $\Delta x = 5\,mm$, are highlighted because the Newton-Raphson scheme only converges until 1e-4 for these cases. So, the nonlinear residual is not exactly zero for the larger time steps. As it will be studied in Sec. 3.4, the Newton-Raphson convergence is highly affected by the chosen welding step. In Tab. 8, it can be seen how the time step does not have a huge influence on the MP dimensions and peak temperature. Therefore, the optimal welding step is the maximum that achieves the Newton-Raphson convergence. In Goldak's model, it is set as $\Delta x = 2\,mm$. Taking into account the Goldak's double ellipsoidal length, $a_f + a_r = 45\,mm$, it is deduced that the heat source needs to be superposed 23 times to accurately reproduce the melt pool.

3.4 Newton-Raphson Convergence

The Newton-Raphson method has been chosen over the Picard's scheme to solve the nonlinear residual from Eq. 31. It has been found that the Picard's method is not converging, possibly due to the highly nonlinear nature of the problem. Thus, to study the Newton-Raphson convergence, the temperature difference norm, $\|\Delta T\|$, has been monitored throughout the iterations in Fig. 9. Besides, the temperature difference convergence rate, CR, has been computed in Tab. 9 for different welding steps Δx.

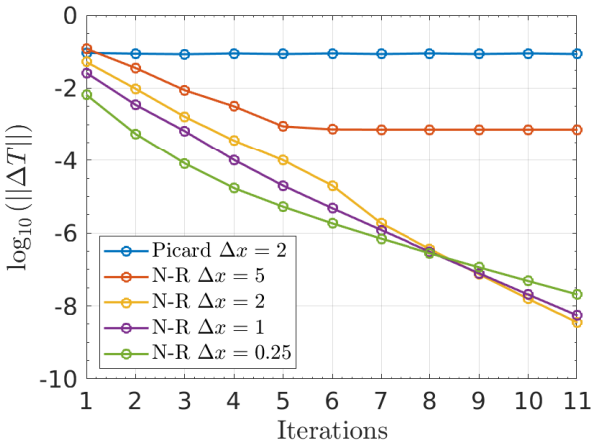

Figure 9: Newton-Raphson convergence study at $t = 15\,s$ using different welding steps Δx in mm.

Iter	$\Delta x = 5$		$\Delta x = 2$		$\Delta x = 1$		$\Delta x = 0.25$	
	$\|\Delta T\|$	CR	$\|\Delta T\|$	CR	$\|\Delta T\|$	CR	$\|\Delta T\|$	CR
1	0.12	-	0.052	-	0.026	-	6.5e-3	-
2	0.035	1.15	9.6e-3	1	3.4e-3	0.82	5.5e-4	0.76
3	8.7e-3	0.72	1.6e-3	0.85	6.5e-4	1.1	8.2e-5	0.83
4	3.2e-3	1.25	3.6e-4	0.83	1.03e-4	0.88	1.7e-5	0.75
5	8.8e-4	0.14	1e-4	1.3	2e-5	0.87	5.3e-6	0.9
6	7.3e-4	0.06	2e-5	1.5	4.8e-6	0.97	1.8e-6	0.92
7	7.2e-4	-	1.8e-6	0.67	1.2e-6	0.99	6.9e-7	0.95
8	7.2e-4	-	3.6e-7	0.99	3.06e-7	0.99	2.8e-7	0.97
9	7.2e-4	-	7.4e-8	0.98	7.8e-8	0.99	1.1e-7	0.97
10	7.2e-4	-	1.5e-8	0.96	2.05e-8	0.98	4.8e-8	0.98
11	7.2e-4	-	3.5e-9	-	6.4e-9	-	2.06e-8	-

Table 9: Temperature difference norm and convergence rate at each Newton-Raphson iteration at $t = 15s$ using different welding steps Δx in mm.

In Fig. 9, it can be seen how the Newton-Raphson method with $\Delta x = 5\,mm$ is not converging after the fifth iteration. Thus, the temperature difference norm is stabilized at 7.2e-4 because the previous time step solution, $\mathbf{T}^n$, is too distant from $\mathbf{T}^{n+1}$. Using smaller welding steps, the temperature difference reaches 1e-8 with 11 iterations. In Tab. 9, it can be observed how the optimal NR quadratic convergence is not achieved. Instead, a linear convergence is obtained probably because the exact Jacobian matrix is not computed when dealing with the liquid fraction derivative (see Sec. 2.5.3). The welding step $\Delta x = 2\,mm$ gives the better convergence, reaching a CR of 1.5 in the sixth iteration. Furthermore, in Fig. 9, the convergence using $\Delta x = 0.25\,mm$ is clearly deteriorated during the last iterations. The number of iterations needed for convergence depends on the problem nonlinearities. Therefore, during the first iterations where there material is not melted, the NR iterations are greatly reduced.

3.5 Goldak's Validation

The results obtained with Goldak's model are presented and compared with the original results from [3]. The melt pool distribution is shown in Fig. 10 using two different views. In addition, the temperature distribution along the top surface width has been plotted in Fig. 11.

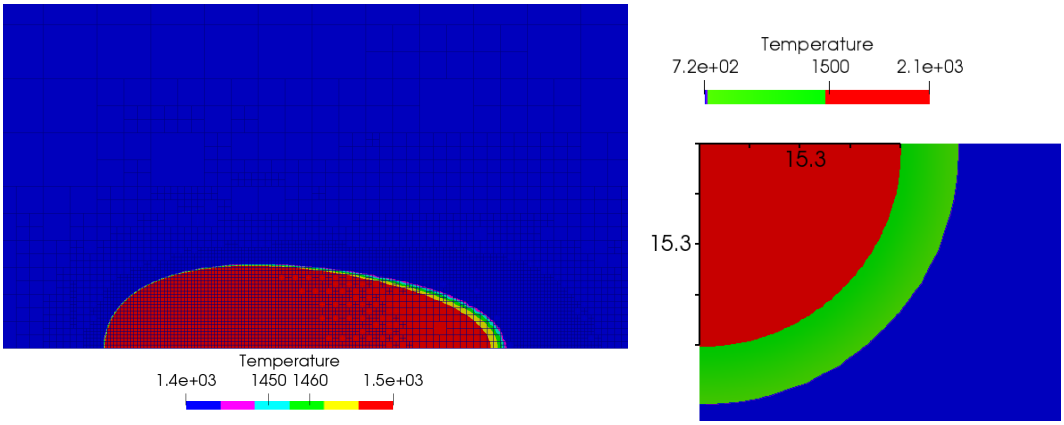

(a) Melt pool view from the top

(b) Melt pool cross section

Figure 10: Goldak's model melt-pool with mesh refinement (a) and depth and width sizes (b).

The melt pool is defined as the region where the local temperature is higher than the liquid temperature (red region in Fig. 10). In Fig. 10 (a), it can be seen how the smaller elements are concentrated at the front of the melt pool, where the solid to liquid phase change happens quicker. On the other hand, at the rear part of the melt pool, the phase change is smoother which induces a smaller temperature gradient in the welding direction. The melt-pool cross section in Fig. 10 (b) can be compared with Goldak's result in Fig. 4. Thus, the MP width measures $15.3\,mm$ while Goldak's fusion zone measures $16\,mm$ and the experimental value is $14\,mm$. Notice that the MP depth is equal to the width because the ellipsoidal parameters b and c are the same in Goldak's analysis. Besides, no heat loses are allowed on the double ellipsoidal surface, so the normal heat flux on the top surface is also zero.

The temperature distribution along the top surface width has been validated against Goldak's results in Fig.11 (a). The solution is computed $57.5\,mm$ behind the laser, meaning that the local ellipsoidal coordinate is equal to $\xi = -57.5\,mm$. It can be seen how the solution matches the experimental distribution outside the melt-pool region, but gives completely different temperature values within the melt pool. One of the reasons could be the radiation and convection boundary conditions, which are imposed differently in Goldak's original model (Sec. 2.6.1). The idea is that the double ellipsoidal top surface is much bigger than the melt pool, so at the end, Goldak's original model is predicting lower loses on the top surface. This could explain the maximum temperature difference in Fig. 11 (a). Besides, the Goldak model solution does not meet the symmetry conditions at $x = 0$, where the normal heat flux should be zero.

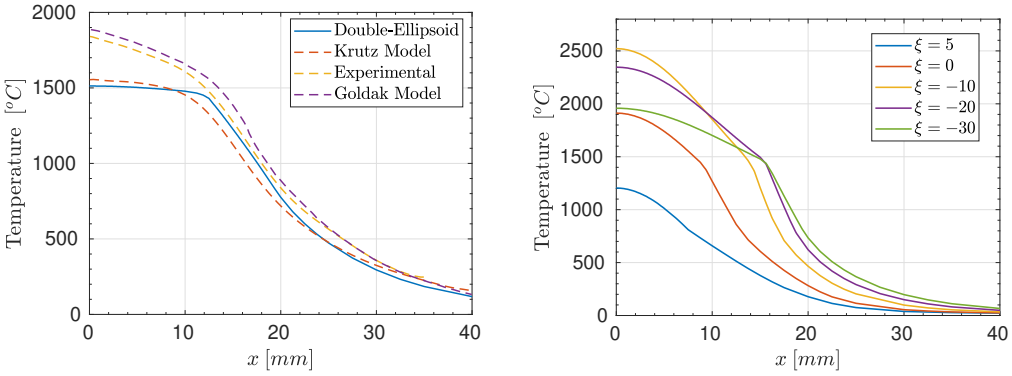

(a) Validation after the heat source has passed ($\xi = -57.5\,mm$)

(b) Solution at different positions, ξ, in mm before and after the heat source

Figure 11: Goldak's model temperature distribution along the top surface width.

In Fig. 11 (b), different ξ locations have been compared to see how the local temperatures distribution changes while the heat source is moving. It can be seen how the peak temperature is not located at the laser spot, but behind it due to the moving heat source. Also, the temperature distribution is not smooth at the phase-change due to the released latent heat. The effect is more pronounced behind the laser, where the phase-change is slower.

3.6 Experimental Validation

The results obtained with the experimental model described in Sec. 2.7 are compared with the melt pool experimental measures in Tab. 11. The melt pool sizes and the peak temperature are computed using the operating conditions detailed in Tab. 10. Furthermore, the melt pool cross section is shown in comparison with the experimental evidence in Fig. 12-14. Finally, the melt pool shape is presented in Fig. 15 for the different experimental tracks.

	Laser Power $[W]$	Laser Speed $[mm/min]$	Laser Radius $[mm]$	MP Depth $[\mu m]$	MP Width $[\mu m]$
Track 10	1000	800	2.5	636.2 ± 55	1346.7 ± 55
Track 14	1500	800	2.5	756.8 ± 55	1763.1 ± 55
Track 17	2000	400	2.5	1535.1 ± 55	2631.5 ± 55

Table 10: Experimental tracks operating conditions and measured melt-pool sizes.

In Tab. 11, the double ellipsoidal model is under-predicting the MP width with a maximum error of 14%, while over-predicting the MP depth with a maximum error of 11%. A priori, one may think that the results could be improved reducing the double ellipsoidal axis b. However, during the calibration process detailed in Sec.

	MP Depth $[mm]$		MP Width $[mm]$		MP Length $[mm]$	Peak Temperature $[°C]$
Track 10	0.635	-0.18 %	1.29	-4.21%	5.2	1983
Track 14	0.82	+8.35%	1.51	-14.3%	5.95	2130
Track 17	1.71	+11.4%	2.3	-12.6%	7.73	2673

Table 11: Melt pool dimensions and peak temperature compared with the experimental evidence.

2.7, it was found that reducing b had almost no effect on the resulting MP depth. Instead, the MP width was slightly increased. Notice that the final MP depth is much bigger than the double ellipsoidal axis b. Overall, the energy absorptivity η is the most sensitive parameter for the MP size. In fact, for Track 10 the absorptivity was set to $\eta = 0.78$, but a smaller value of $\eta = 0.6$ was needed for Track 14 and 17 to match the experimental results.

The qualitative results in Fig. 12-14 show a good agreement with the experimental evidence. However, it can be observed that the experimental melt pool presents a steeper shape at the top surface. Regarding the results in Fig. 15, it can be seen how the melt pool sizes increase proportionally to the laser power, showing a similar shape but with bigger sizes (Track 10 and 14). Nevertheless, when the scanning speed is reduced, the melt pool becomes thicker presenting a more circumferential cross section (Track 17). This happens because the resulting power density introduced by the laser is increased during the same time step.

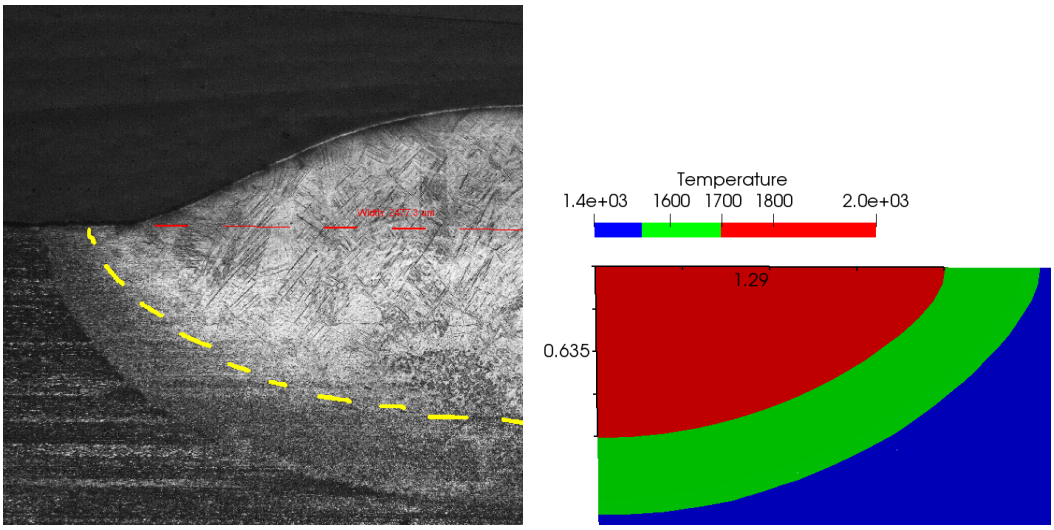

Figure 12: Track 10 melt pool cross section comparison between experimental evidence and simulation results.

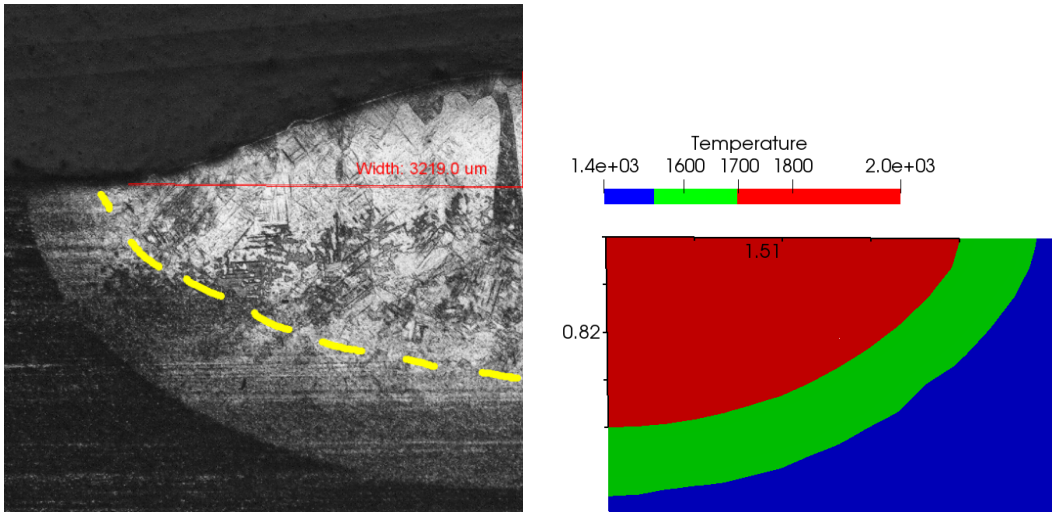

Figure 13: Track 14 melt pool cross section comparison between experimental evidence and simulation results.

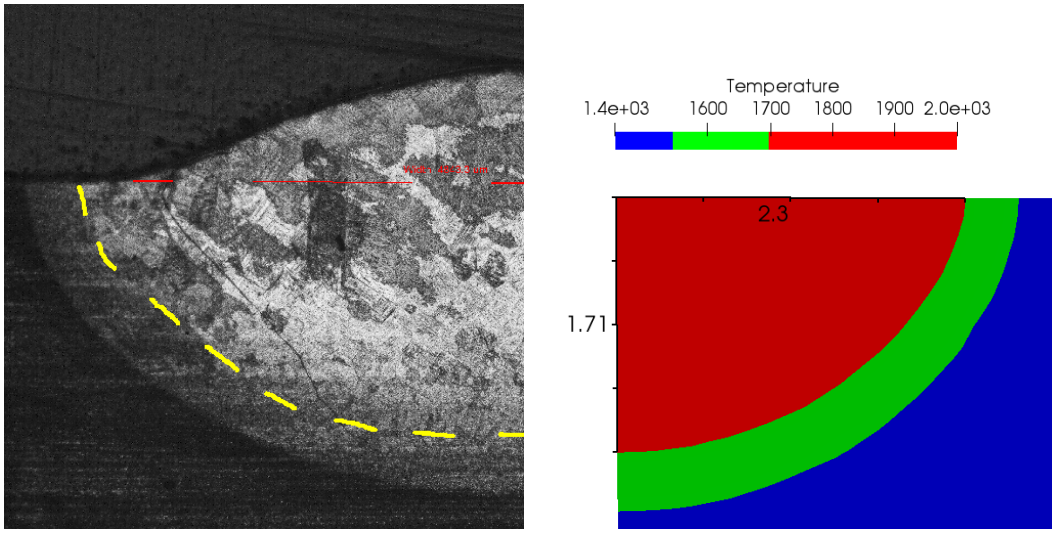

Figure 14: Track 17 melt pool cross section comparison between experimental evidence and simulation results.

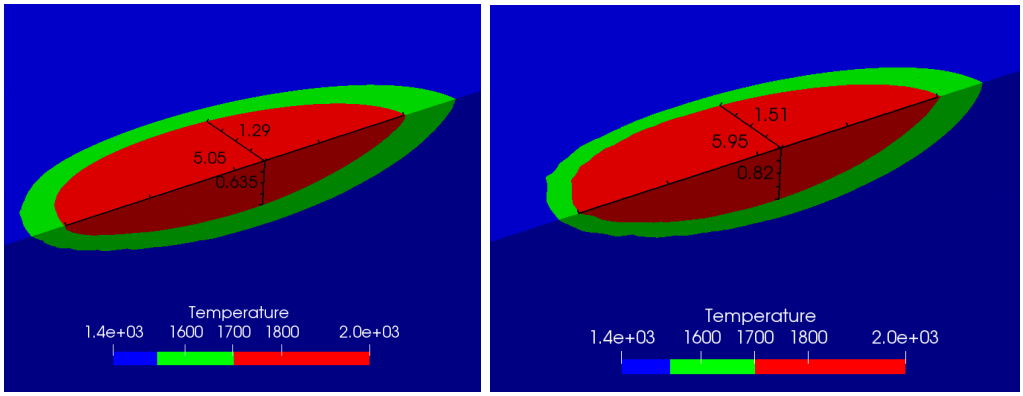

(a) Track 10

(b) Track 14

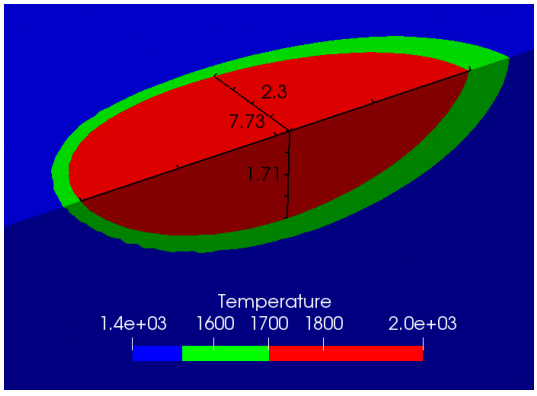

(c) Track 17

Figure 15: Melt pool shape with depth, width and length sizes in mm for different experimental tracks.

4 Conclusions

A numerical tool to predict the melt-pool shape in AM processes has been developed. The computational model has been successfully verified and validated against the available experimental evidence. It has been found that the mesh resolution around the melt pool is crucial to obtain a consistent definition of the double ellipsoidal heat source. Besides, the minimum element size needs to be small enough to accurately solve the phase-change interface. Furthermore, given the highly nonlinear nature of the problem, the maximum welding step is restricted to achieve the Newton-Raphson convergence.

The model's ability to predict the melt pool width and depth has been proven with a maximum error of 14%. Beforehand, the double ellipsoidal parameters need to be calibrated to match the experimental results. In this regard, the energy absorptivity is found to be the most sensitive parameter for the predicted melt pool sizes. Compared with Goldak's results, the presented model is clearly not suited to predict the temperature distribution at the melt pool tail. However, more details about Goldak's original results would be needed to extract further conclusions.

The melt-pool in DED processes presents a slender shape which grows more or less proportionally in all directions with the laser input power. However, when reducing the scanning speed, the molten pool becomes thicker presenting a more circumferential cross section.

References

[1] Sing SL, Tey CF, Tan JHK, Huang S, Yeong WY. 3D printing of metals in rapid prototyping of biomaterials: Techniques in additive manufacturing. In: Narayan R, editor. Rapid Prototyping of Biomaterials (Second Edition). second edition ed. Woodhead Publishing Series in Biomaterials. Woodhead Publishing; 2020. p. 17–40. Available from: https://www.sciencedirect.com/science/article/pii/B9780081026632000022.

[2] Franco R, Loaiza WG, Lean PP, Yépez H. A one way coupled thermo-mechanical model to determine residual stresses and deformations in butt welding of two ASTM A36 steel plates;. Available from: http://investigacion.pucp.edu.pe/grupos/inacom/.

[3] Goldak J, Chakravarti A, Bibby M. A New Finite Element Model for Welding Heat Sources.

[4] Wei HL, Mukherjee T, Zhang W, Zuback JS, Knapp GL, De A, et al.. Mechanistic models for additive manufacturing of metallic components. Elsevier Ltd; 2021.

[5] Carraturo M. Modelling, Validation, and Design for Additive Manufacturing Applications of Numerical methods to 3D printing processes; 2019.

[6] Chiumenti M, Cervera M, Dialami N, Wu B, Jinwei L, Agelet de Saracibar C. Numerical modeling of the electron beam welding and its experimental validation. Finite Elements in Analysis and Design. 2016 nov;121:118–133.

[7] Varona T. Sensitivity analysis and experimental calibration for the Additive Manufacturing computational framework; 2016.

[8] Buckley DO. Solution of Nonlinear Transient Heat Transfer Problems. Florida International University; 2010. Available from: https://digitalcommons.fiu.edu/etd/302.

[9] Chiumenti M, Cervera M, Salmi A, Agelet de Saracibar C, Dialami N, Matsui K. Finite element modeling of multi-pass welding and shaped metal deposition processes. Computer Methods in Applied Mechanics and Engineering. 2010 aug;199(37-40):2343–2359.

[10] Joan Baiges, Camilo Bayona. Refficientlib: an efficient load-rebalanced adaptive mesh refinement algorithm for high-performance computational physics meshes. SIAM journal on scientific computing. 2017;39:C65–C95.

[11] Lu X, Chiumenti M, Cervera M, Li J, Lin X, Ma L, et al. Substrate design to minimize residual stresses in Directed Energy Deposition AM processes. Materials and Design. 2021 apr;202.